American Institute of Aeronautics and Astronautics

AIAA 2002-2418

Finite Element Modeling of the NASA Langley Aluminum Testbed Cylinder

Ferdinand W. Grosveld
Lockheed Martin Engineering and Sciences

Jocelyn I. Pritchard, Ralph D. Buehrle and Richard S. Pappa
NASA Langley Research Center
Hampton, Virginia

8th AIAA/CEAS Aeroacoustics Conference

June 17-19, 2002 / Breckenridge, Colorado

FINITE ELEMENT MODELING OF THE NASA LANGLEY ALUMINUM TESTBED CYLINDER

Ferdinand W. Grosveld*
Lockheed Martin Engineering and Sciences
NASA Langley Research Center
Hampton, VA 23681

Jocelyn I. Pritchard†
Ralph D. Buehrle‡
Richard S. Pappa§
NASA Langley Research Center

Abstract

The NASA Langley Aluminum Testbed Cylinder (ATC) was designed to serve as a universal structure for evaluating structural acoustic codes, modeling techniques and optimization methods used in the prediction of aircraft interior noise. Finite element models were developed for the components of the ATC based on the geometric, structural and material properties of the physical test structure. Numerically predicted modal frequencies for the longitudinal stringer, ring frame and dome component models, and six assembled ATC configurations were compared with experimental modal survey data. The finite element models were updated and refined, using physical parameters, to increase correlation with the measured modal data. Excellent agreement, within an average 1.5% to 2.9%, was obtained between the predicted and measured modal frequencies of the stringer, frame and dome components. The predictions for the modal frequencies of the assembled component Configurations I through V were within an average 2.9% and 9.1%. Finite element modal analyses were performed for comparison with 3 psi and 6 psi internal pressurization conditions in Configuration VI. The modal frequencies were predicted by applying differential stiffness to the elements with pressure loading and creating reduced matrices for beam elements with offsets inside external superelements. The average disagreement between the measured and predicted differences for the 0 psi and 6 psi internal pressure conditions was less than 0.5%. Comparably good agreement was obtained for the differences between the 0 psi and 3 psi measured and predicted internal pressure conditions.

Introduction

The Structural Acoustics Branch at NASA Langley Research Center initiated the design and construction of an Aluminum Testbed Cylinder (ATC) to create a universal structure for evaluating structural acoustic codes, modeling techniques and optimization methods used in the prediction of aircraft interior noise. The purpose of the current program is to develop high fidelity, manageable ATC numerical models based on accurate geometric, structural and material properties of the participating components. The component structures, up to complete fuselage configurations, require experimental validation performed on the physical model. Recent numerical modeling and vibro-acoustic modal testing pursued at the NASA Langley is listed in References 1-8. This report discusses the finite element model development and validation of three isolated components and six assembled configurations through comparison with modal frequencies from experimental modal surveys. Updated and refined finite element models that exhibit increased correlation with the measured modal data are discussed.

Aluminum Testbed Cylinder

The Aluminum Testbed Cylinder (ATC), shown in Figure 1, was designed as a simplified model of an aircraft fuselage structure. Six configurations of component assemblies were considered (Table1). The bare frame substructure of Configuration I includes longitudinal stringers, ring frames and end rings. The cylindrical section of the testbed with the longitudinal stringers is 144 inches long with a diameter of 48 inches. Nine aluminum ring frames are evenly spaced over the length of the cylinder and twenty-four stringers are equally distributed around the circumference. The aluminum end rings have a 2-inch by 1.5-inch cross-section. Configuration II adds a plate to each end of the bare frame cylinder section (Table 1). Each end plate consists of a two-inch-thick particleboard with a half-inch-thick piece of plywood attached. Configuration III in Table 1 constitutes the bare frame, without the end plates, but covered with a 0.040-inch thick aluminum skin. The skin is assembled from four 144-inch-long overlapping aluminum sheets. Configuration IV includes the bare frame, the skin and the end plates. One-quarter inch thick fiberglass-reinforced epoxy composite domes, featuring pressure release devices and access plates, are

*Aerospace Engineering Manager, Associate Fellow
†Research Engineer, Structural Dynamics Branch
‡Senior Research Engineer, Structural Acoustics Branch
§Senior Research Engineer, Structural Dynamics Branch, Member

installed in Configuration V to facilitate pressurization (up to 7 psi) and wind tunnel testing (Figure 1). Pressure differential loadings are applied to the ATC in Configuration VI.

Experimental Modal Analysis

Component Surveys

Modal survey measurements were conducted on an isolated longitudinal stringer, a ring frame and a pressure dome. Each component was suspended from bungee chords to simulate free-free conditions. The modal parameters were obtained from a modal analysis of the frequency response functions between reference accelerometers and a hammer impact force. Several impact locations were used to capture the modal properties for the first ten to sixteen modes. The polyreference curevefitter in the Spectral Dynamics STAR software was used to determine the modal properties from the frequency response data. The modal results were used to validate the finite element models of the components.

Configuration Surveys

Experimental modal surveys were performed[3,8] by the NASA Langley Structural Dynamics Branch on the six ATC configurations in Table 1. Bungee chords were used to simulate free-free boundary conditions for the first three ATC configurations. The ATC was supported on four airbag isolators for the other configurations to accommodate the increased weight of the test structure and provide more stability to the setup. Figure 2 shows the setup for the modal tests on the fully assembled ATC (Configuration V). Four shakers were used simultaneously for all tests. Figure 3 shows a close-up of one of the shakers in the test setup. Another shaker is located in the background. The two other shakers in the experiment are located on the opposite side of the cylinder. One shaker was used to apply a tangential side force at a 45-degree angle, primarily exciting the torsional and axial modes of the structure. The other three shakers excited the cylinder in the radial direction to force participation of the bending and shell modes of the structure. Continuous random signals were used as input to the four shakers. A data acquisition system (DAS) was employed to record two hundred twenty-eight response measurements and four signals of the excitation inputs. The force and acceleration time histories were recorded on several analog-to-digital converter throughput disks in the DAS, where anti-aliasing and autoranging capabilities ensured high quality measurements. The frequency response functions featured 12,800 lines over a frequency range from 0 to 1000 Hz, resulting in a resolution of 0.078125 Hz. The functions were generated using seventy-five ensemble averages. Mode Indicator Functions (MIF) were calculated from the frequency response functions to provide an estimate of the natural vibration frequencies of the structure. The Eigensystem Realization Algorithm (ERA) was used to identify the modal parameters (natural frequencies, damping factors, and mode shapes) for each test configuration.[3,8] Damping factors were obtained for all modes but are not listed in this paper.

Component Finite Element Models

Geometry and finite element models, including material properties, element properties and boundary conditions were developed and pre-processed in MSC.PATRAN. The ATC finite element model was assembled from component models of the longitudinal stringers, ring frames, end rings, end plates, shell, and domes (including end cap rings and access plates). The finite element model was equivalenced to remove redundant nodes. A structural damping factor of 0.01 was employed for all frequencies. Spherical coordinate systems were used in the analyses of the dome assemblies and cylindrical coordinate systems were used for the analyses of all other components. Normal mode studies were performed in MSC.NASTRAN up to 400 Hz to obtain the structural modal parameters. The modal data were analyzed in the post-processor MSC.PATRAN. Global cylinder beam modes included torsion, shearing, axial and bending modes. The circumferential-axial modal frequencies were identified by mode shape and mode number. The index 'i' indicated the number of circumferential waves in the mode shape while the index 'j' specified the number of axial half-waves.

Longitudinal Stringers

Beam Model - Each of the twenty-four aluminum longitudinal hat stringers measured 143.5 inches long with a 0.1515 in^2 cross-sectional area. The stringers were initially modeled[1] by eighty CBEAM tapered beam elements. PBEAM cross-sectional properties included area, moments of inertia, inertia product, the torsional constant, angle to the primary axis of bending, shear center and neutral axis location offsets, shear stiffness and warp coefficients. Aluminum material properties included an elasticity modulus $E=9.9\ 10^6$ psi, a shear modulus $G=3.8\ 10^6$ psi, a Poisson's ratio $\nu=0.33$ and a specific weight $g\rho_s=0.0978$ pci. These material properties were used

consistently for all aluminum substructures. Vectors were defined for the beam elements on each stringer to define their proper orientation. The elements of the beam model were offset to position the base of each stringer flush with the 24-inch radius of the cylinder. The finite element model of the isolated stringer was compared with experimental modal survey data in Reference 1. Modal frequencies were overpredicted by an average of 7.5% and a maximum of 16.4% for the first twelve modes. Overprediction of these frequencies indicated that the beam element model was stiffer than the physical structure. Modeling the stringers by one-dimensional beam elements resulted in stringer distances that were larger in the ATC finite element model than in the physical model.

Plate Model - The beam model was updated to a plate element model, which had been proven to be less stiff for a ring frame model in Reference 1. The two-dimensional plate elements are able to represent the width of the stringers, yielding the same stringer distance in the numerical and physical models. Each updated hat-shaped stringer finite element model consisted of four hundred thirty-four CQUAD4 elements with five hundred four nodes and 2520 degrees of freedom. The plate elements were 0.060 inch thick and were assigned aluminum material properties. The numerically computed modal frequencies are compared with the experimental data in Table 2. Good agreement was obtained within an average 2.8% and a maximum 4.3% of the measured modal frequencies for the first twelve modes.

Refined Model - The fidelity of the finite element model was improved by doubling the number of plate elements. This convergence resulted in better agreement with the measured data to within an average of 2.1% and a maximum of 3.7% as shown in Table 2. The consequence of increasing the number of elements was that not only the stringer model became larger but also that the models of connecting components needed to be updated with a higher number of elements. A total of 32,592 CQUAD4 plate elements were used to model the twenty-four longitudinal stringers.

Ring Frames

Hybrid Model - The nine aluminum J-section ring frames had a cross-sectional area of 0.3537 in^2 and an outer radius of 24 inches. Modal frequencies for the isolated ring frame had been predicted with all-beam element and all-plate element models in Reference 1, but had resulted in poor comparison with measured modal frequencies. Since the all-beam element model was stiffer than the actual ring frame and the all-plate element model did not provide enough stiffness, a hybrid model was developed combining the one- and two-dimensional models. The web of the J-section ring frame was modeled with plate elements while beam elements were used for the flanges of the ring frame. Tapered beams were used to include shear center offsets, neutral axis offsets and warping coefficients. The elements of the beam model were offset to position the outer radius of each frame flush with the 24-inch cylinder radius. Vectors were defined for the proper orientation of the beam elements. The hybrid model of the ring frame consisted of two hundred sixteen QUAD4 and two hundred eighty-eight CBEAM elements with four hundred fifty-eight nodes for 2472 degrees of freedom. The modal frequencies for the hybrid model were predicted[1] within an average 4.3% and a maximum 7.6% of the measured modal data.

Updated Hybrid Model - The distance between the one-dimensional beam elements of two ring frames models was larger than the width between two ring frames modeled by two-dimensional plate elements. The hybrid model of the ring frame was therefore updated with CQUAD4 plate elements for the flanges atop the J-section to ensure the proper ring frame distance. The CQUAD4 elements were 0.125-inch thick except for a span of 0.35 inch on either side of the U-shaped cutouts where the thickness was 0.063 inch to accommodate the 0.06-inch thick longitudinal stringer. CQUAD4 elements were also used to model the 0.1-inch thick web of the J-stringer down to the bottom line of the U-shaped cutouts (Figure 5). The L-shaped part of the ring frame below the cutout was modeled with tapered CBEAM elements. The beam elements had a 0.116 in^2 cross-sectional area. The total number of four hundred thirty-two CQUAD4 elements and one hundred sixty-eight CBEAM elements combined to an estimated 3,033 degrees of freedom for each ring frame. Aluminum material properties were assumed for all elements. Predictions of the modal frequencies were within an average 4.7% and within a maximum 6.7% of the measured modal frequencies (Table 3).

Refined Hybrid Model - The number of elements in the hybrid model was doubled to match the number of nodes at the junction points with the longitudinal stringers (refined stringer model). The modeling of the hybrid ring frame had indicated that the beam elements were too stiff while the plate elements did not provide enough stiffness to the ring frame. Correlation with the experimental modal frequencies was improved by optimizing the J-stringer areas for which plate elements and beam elements were used. Different locations of

the beam elements below the U-shaped cutouts were modeled. Modal frequencies were computed and compared with the measured modal data. Best agreement was obtained for the beam elements modeled 0.2 inches below the U-shaped cutouts. The nine ring frames were modeled with a total of 3,024 CBEAM and 2,304 CQUAD4 elements. The predicted modal frequencies of the refined ring frame models were within an average 1.5% and within a maximum 2.6% of the measured modal frequencies (Table 3).

End Rings

The ring frame at each end of the cylinder was initially modeled[1] using CBAR elements with a cross-sectional area of 3.0 in^2. The simpler CBAR elements instead of CBEAM elements could be used as the shear center axis and neutral axis for rectangular cross-sections coincide. The one-dimensional bar elements do not have a geometrical thickness yielding a wider bay area between the ring frames and the end frames of the cylinder. Solid elements for the end ring frames were introduced in an updated model to ensure the proper width of the bay area and to more accurately model the cross-sectional geometry. The number of elements was increased to match the number of nodes at the junction points of the shell and the longitudinal stringers. The 3840 CHEXA solid elements were assigned aluminum material properties and yielded an approximate 36,000 degrees of freedom for each end ring. No modal testing was performed on the end ring as a single component.

Shell

The number of the quadrilateral CQUAD4 plate elements for the shell was doubled in two directions to match the increased number of nodes at the junction points with the longitudinal stringers and the ring frames. The mesh representing the cylinder shell was modeled with a total of 56,064 CQUAD4 elements for the skin along with four hundred thirty-two CTRIA3 elements for connectivity to the end rings. The shell was not tested as an individual component.

End Plates

The end plates consisted of a half-inch thick plywood panel mounted onto two-inch thick particleboard. The particleboard was chosen for its high density, high rigidity and low cost. Two circular patterns of twenty-four equidistant half-inch holes were drilled at radii of 7.5 and 9 inches from the center. The openings allow the pressure on both sides of the end plates in Configuration VI to equalize during pressurization tests. The end plates were initially modeled with 1184 CTRIA3 elements[1] having particleboard material properties and an inflated thickness to account for the plywood panel. The particleboard and plywood were remodeled as individual panels using CHEXA solid elements to increase accuracy. The number of elements was increased to match the number of nodes at the junction grid points with the stringers, the shell and the end rings. The particleboard had an elasticity modulus $E_{pb}=2.1755\ 10^6$ psi, a Poisson's ratio $\nu_{pb}=0.33$ and a specific weight $g\rho_{pb}=0.0284$ pci. The plywood featured an elasticity modulus $E_{pw}=1.2\ 10^6$ psi, a Poisson's ratio $\nu_{pw}=0.33$ and a specific weight $g\rho_{pw}=0.0191$ pci. The particleboard panels were modeled with a total of 3,072 CHEXA elements while 2,304 CHEXA elements were used for the plywood panels. No experimental modal data were available for comparison.

Domes

The S-fiberglass composite end domes feature a high stiffness-to-weight ratio and were designed to be sufficiently strong to safely carry the pressure loading during pressure testing. End cap rings supported and strengthened the rim of each dome. Access ports with a 10-inch diameter were installed in the center of each dome to accommodate devices that will regulate the interior pressure conditions. The end cap rings and access ports were initially considered part of the dome and were not individually modeled[1]. The domes were remodeled with separate components for the dome, the dome rings and the access plates to increase the fidelity of the model. The two 0.5-inch thick aluminum access plates were represented by eight hundred sixty-four CQUAD4 plate elements. The two domes consisted of a total of 9,408 CQUAD4 elements. Plate element offsets were applied to account for the proper center plane locations. The S-fiberglass and epoxy matrix mechanical properties are listed in Table 4. The lamina composite properties were obtained by proportioning the S-fiberglass and epoxy matrix mechanical properties with respect to relative volume. The lamina composite mechanical properties are tabulated in Table 4. The laminate mechanical properties were computed in MSC.PATRAN for the stacking sequence in Table 5 resulting in $E_{xx}=4.55\ 10^6$ psi, $E_{yy}=2.10\ 10^6$ psi, $G_{xy}=1.20\ 10^6$ psi and $\nu_{xy}=0.432$. The dome end frames were modeled with three hundred eighty-four CHEXA solid elements. The solid elements combined the aluminum properties of the 0.375 inch-thick dome end frame and the material properties of the 0.25-inch thick fiberglass dome edge material. The mechanical properties for the composite of the two materials were calculated using volume proportionality

(V_a=0.6 and V_e=0.4) resulting in E_{ae}=7.26 10^6 psi, G_{ae}=2.74 10^6 psi and ν_{ae}=0.322. Modal frequencies and mode shapes were computed for finite element models of the isolated fiberglass domes with the dome end frames and access plates installed. The predicted modal frequencies were within an average 2.9% and a maximum 5.6% of the measured modal data for the first six circumferential modal pairs. The results are shown in Table 6.

ATC Finite Element Configurations

Finite element modal frequency predictions were made for the six assembled ATC component configurations for comparison with measured modal data. Models were updated and refined to increase agreement between numerical and experimental modal results.

Configuration I

The stringer, frame and end ring components were assembled to form ATC Configuration I before the number of elements was doubled (unrefined) and after the number of elements was doubled (refined). Mode numbers of sixty-one mode shapes were identified up to a frequency of 150 Hz. The refined and unrefined predicted modal frequencies are compared with the measured data of the first seventeen modes in Table 7. The modal frequencies of the unrefined model were overpredicted by an average 9.6% and a maximum 15.2% of the experimental modal frequencies. The refined model was expected to increase accuracy but underpredicted the measured modal frequencies by an average of 10.6% and a maximum of 23.9%. The underprediction suggested a cylinder model with less inherent stiffness. By increasing the number of elements in the components, the number of congruent nodal points at the junctions of the stringers and the frames were increased from twelve to thirty nodes. Figure 5a shows a schematic of the junction between the unrefined hat-section longitudinal stringer and the unrefined J-section ring frame where the components were connected by twelve nodes. By doubling the number of elements for the stringers and the frames the number of congruent nodes at the junctions increased from twelve to thirty as illustrated in Figures 5b. The thirty-node junction allowed more degrees of freedom and exhibited less rigidity, which resulted in lower modal frequencies. The refined stringers and refined ring frames were subsequently modeled to connect at only six node locations as illustrated in Figure 5c. Agreement between the predicted modal frequencies with these six-node junctions and the measured modal frequencies improved considerably as evidenced in Table 7. The predicted modal frequencies were within an average 4.4% and a maximum of 7.5% of the measured data. It was concluded that a lower number of connected nodes at the junctions of the longitudinal stringers and the ring frames resulted in less flexible substructure assemblies with associated higher modal frequencies. It should be noted that the layout of the node connections and the number of elements changed for each of the three configurations in Figures 5a, 5b and 5c, which also affected the rigidity of the junction. The plate elements at the junctions of the refined longitudinal stringers and refined ring frames were remodeled with twelve common nodes at approximately the same locations as the rivets that connect the stringers and the frames in the hardware model. The modal frequencies predicted for the improved model with the twelve-node junctions are compared with the measured data from the modal surveys in Table 8. The predicted modal frequencies were within an average 2.9% and a maximum of 5.1% of the measured data.

Configuration II

Predictions up to a frequency of 350 Hz were made for Configuration II with the twelve common nodes approximately at the hardware model rivet locations. One hundred-forty predicted modes were compared with seventy-seven experimental modal frequencies up to 245 Hz. A comparison for the first seventeen modal frequencies is shown in Table 9. The predicted modal frequencies were within an average 3.7% and a maximum 6.5% of the measured data.

Configuration III

The cylinder skin was added in Configuration III. The number of CQUAD4 elements for the shell was doubled in two directions to match the increased number of elements in the refined stringer and refined ring frame models. Thirty-nine modal frequencies were predicted and identified by mode shape for frequencies up to 352 Hz. The first seventeen measured and predicted modal frequencies are compared in Table 10. The predicted modal frequencies were within an average 4.4% and a maximum 9.9% of the measured data.

Configuration IV

Twenty-six predicted and measured modal frequencies up to 400 Hz were compared for Configuration IV, which included the ring frames, longerons, skin, end rings and end caps. The results and error values for the first seventeen modes are tabulated in Table 11. The experimental modal frequencies for Configurations IV

through VI were obtained for free boundary conditions simulated by suspension on four air-bag isolators. The predicted modal frequencies were within an average 5.3% and a maximum of 13.9% of the measured data.

Configuration V

The domes were added to the model of Configuration IV including a 0.09-inch wide and 0.625-inch deep radial outside gap between the dome ring and the cylinder end rings. Detailed inspection of the test article had revealed that the dome rings were attached to the cylinder end rings in a radial direction but not in the axial direction. This gap was larger than the equivalencing tolerance used in MSC.PATRAN preventing two opposite nodes from being merged when using the equivalencing feature. A comparison of the first seventeen predicted and measured modal frequencies is listed in Table 12. The predicted modal frequencies were within an average 9.1% and a maximum of 25.3% of the measured data. It was concluded from Table 12 that the lowest order circumferential modes and the first bending modes showed the highest discrepancies between predictions and measurements. It was hypothesized that this could be due to boundary conditions that were too stringent at the end of the cylinder where the domes were attached. Indeed, leaving out the gap modeled between the dome and cylinder end rings caused the modal frequencies to be raised even higher. A more thorough inspection of the physical connection between the domes and the cylinder will be performed when the cylinder structure is dismantled. One hundred nineteen modes up to 400 Hz were predicted by the finite element analysis while twenty-four modes were identified up to 290 Hz from the experimental modal survey. Fifty-seven of the predicted modes were related to the fundamental modes of the cylinder bays bounded by the ring frames and longerons at frequencies higher than 350 Hz. The cylinder bays are subjected to different boundary conditions for each circumferential-axial cylinder mode shape. The cylinder bay modes occur therefore at a multitude of frequencies, each of which is related to a specific global mode shape of the ATC cylinder structure.[1] Post-processing and identification analysis also yielded eight stringer modes that were related to the vibration of the cylinder as a single structure.

Configuration VI

Pressure differential loadings of 3 psi and 6 psi were incorporated in the finite element model of Configuration VI. The MSC.NASTRAN 'STATSUB' command was used for the computation of the normal modes. The command selects the static solution to form the differential stiffness for the elements with the pressure loads. However, MSC.NASTRAN does not allow the processing of models with beam element offsets. The nine ring frames of the ATC were modeled with beam element offsets to position the shear center axis at the appropriate location relative to element grid points. These offsets were an integral part of the modeling of the ring frames and were key for obtaining good comparison between measured and the numerically calculated modal frequencies. The beam offset vectors are treated like rigid elements in MSC.NASTRAN and remain parallel to their original locations making them not suitable for differential stiffness calculations. Even when the pressure loading was applied to only the shell and not the beam elements, the beam elements were still part of the MSC.NASTRAN run and caused a fatal error. An alternative approach was considered creating superelements for the ring frames that would contain the offsets but would be analyzed separately from the residual structure. Superelements are normally used as Main Bulk Data Superelements or PARTS, which allow partitioned input files. However, MSC.NASTRAN would still attempt to do an analysis of the upstream superelement when using the 'STATSUB' command and thus encounter the same incompatibility with the offsets of the beam elements. The solution was found in the implementation of external superelements. The initial normal mode calculations of the ring frames superelement were performed outside the main finite element program and the resulting matrices were stored in an '.op2' output file. Modal frequencies obtained for the external superelement were verified to be the same as for the individual ring frame modal frequencies. The superelement output file was then used as input to the bulk data file of the residual structure. Modal frequencies for the combination of residual structure and external superelement were confirmed to be the same as for the original ATC cylinder with the ring frames. The pressure differential loadings of 3 psi and 6 psi were applied only to the shell elements of the ATC. The model was prepared in MSC.PATRAN for a linear static analysis and an input bulk data file was compiled. The bulk data file was manually modified to perform the normal mode analysis with the calculated differential stiffness by adding a new subcase with the STATSUB command. The predicted modal frequencies for 0 psi, 3 psi and 6 psi were compared with experimental modal survey data for the same conditions. Excellent agreement was obtained when comparing the numerical and experimental differences in modal frequencies for the 0 psi and 6 psi pressurization conditions (Table 13). The average

disagreement between the measured and predicted differences was 0.5% and the maximum disagreement was 1.2%. Equally good agreement was obtained for the differences between the 0 psi and 3 psi internal pressure conditions, although the results are not tabulated here. Pressure differential loadings were applied to the dome elements in addition to the shell elements causing only a negligible shift (less than 0.3%) in the predicted modal frequencies.

Acoustic Normal Modes

The interior of the ATC was modeled by 5184 solid finite elements in MSC.PATRAN. The neutral file of the model was imported into COMET/Vision for pre-processing. The resulting file was executed in COMET/Acoustics to calculate fifty acoustic modes up to a frequency of 600 Hz. Post-processing was performed in COMET/Vision to identify the modal frequencies by mode shape. The first seventeen modes are listed in Table 14 along with half-wavelength mode numbers in axial and circumferential directions. The first radial acoustic mode was predicted at 345.1 Hz. Preliminary acoustic measurements were conducted with a loudspeaker and a microphone. An amplified white noise signal was used as input to the speaker located in the center of one end plate and was measured by a microphone in the center of the opposite end plate. Frequencies with peaks in the narrow-band spectrum correlated well with the first five predicted axial modal frequencies (Table 14). A more detailed experimental modal survey is planned to validate the acoustic finite element model. The validated structural and acoustic finite element models will be used to develop COMET/Acoustics finite element and boundary element models for predicting the coupled structural acoustic response in the interior of the built-up ATC.

Summary

Finite element modal analyses for free boundary conditions were performed on a longitudinal stringer, a ring frame, a pressure dome, and six component assembly configurations of the Aluminum Testbed Cylinder (ATC) for comparison with experimental modal frequencies. Free boundary conditions for the modal tests were simulated by bungee cord suspension of each isolated component and the component assembly Configurations I through III. The stringers were updated from beam to plate element models and refined by doubling the number of elements. Excellent agreement was obtained within an average 2.1% and a maximum 3.7% of the measured modal frequencies. The hybrid ring frames were optimized by adjusting the area represented by the plate elements and remodeling the relocated beam elements. The frames were refined by doubling the number of elements. The predicted modal frequencies were within an average 1.5% and within a maximum 2.6% of the measured modal frequencies. The fiberglass composite domes, the dome end cap rings and the dome access ports were individually modeled with appropriate material properties to increase model fidelity. Predicted modal frequencies were within an average 2.9% and a maximum of 5.1% of the measured data. The end rings, shell and end plates were remodeled to reflect the increase in elements of the refined stringers, frames and domes. The increased number of grid points at the junctions of the refined stringers and frames resulted in less stiff component assemblies with associated lower modal frequencies. The junctions were remodeled to have only twelve instead of thirty common nodes at approximately the same locations as the rivets in the hardware model. Good agreement was obtained for Configurations I, II and III as predicted modal frequencies were within an average 2.9%-4.4% and a maximum 5.1%-9.9% of the measured data. The experimental boundary conditions for configurations IV through VI were simulated by a four air-bag isolator support. Predictions for Configurations IV and V were within an average 5.3%-9.1% and a maximum 13.9%-25.3% of the measured modal frequencies. Modal frequencies were predicted for 3 psi and 6 psi internal pressurization conditions in Configuration VI. Modal frequencies were predicted by applying differential stiffness to the elements with pressure loading and shielding beam elements with offsets from direct calculation by external superelements. The average disagreement between the measured and predicted differences for the 0 psi and 6 psi internal pressure conditions was less than 0.5% and the maximum disagreement was 1.2%. Equally good agreement was obtained for the differences between the 0 psi and 3 psi internal pressure conditions. Pressure differential loadings were applied to the dome elements in addition to the shell elements causing only a negligible shift (less than 0.3%) in the predicted modal frequencies.

Acknowledgments

The finite element model development in this study was performed under Contract NAS1-00135, Task Order 13RBF, “Structural Acoustic Modeling and Laboratory Support,” Dr. Richard J. Silcox, Technical Monitor, National Aeronautics & Space Administration, Langley Research Center, Hampton, Virginia.

References

1. Grosveld, F. W., "Structural Normal Mode Analysis of the Aluminum Testbed Cylinder," AIAA Paper 98-1949, Proceedings of the 39th AIAA/ASME/ASCE Structures, Structural Dynamics, and Materials Conference, Long Beach, CA, April 1998.

2. Fleming, G. A., Buehrle, R. D., and Storaasli, O. L., "Modal Analysis of an Aircraft Fuselage Panel Using Experimental and Finite Element Techniques," Proceedings of the 3rd International Conference on Vibration Measurements by Laser Techniques, Ancona, Italy, June 1998.

3. Pappa, R. S., Pritchard, J. I., and Buehrle, R. D., "Vibro-Acoustics Modal Testing at NASA Langley Research Center," NASA/TM-1999-209319, May 1999.

4. Buehrle, R. D., Fleming, G. A., Pappa, R. S., and Grosveld, F. W., "Finite Element Model Development and Validation for Aircraft Fuselage Structures," Proceedings of the 18th International Modal Analysis Conference, San Antonio, Texas, February 7-10, 2000.

5. Buehrle, R. D., Fleming, G. A., Pappa, R. S., and Grosveld, F. W., "Finite Element Model Development for Aircraft Fuselage Structures," Sound and Vibration Magazine, January 2001, Acoustical Publications, Inc.

6. Buehrle, Ralph D., Robinson, Jay H. and Grosveld, Ferdinand W., "Vibro-Acoustic Model Validation for a Curved Honeycomb Composite Panel," AIAA Paper 2001-1587, 42nd AIAA/ASME/ASCE/AHS/ASC Structures, Structural Dynamics, and Materials Conference, Seattle, WA, 16-19 April 2001.

7. Grosveld, Ferdinand W., Buehrle, Ralph D. and Robinson, Jay H., "Numerical and Acoustic Modeling of a Curved Composite Honeycomb Panel," AIAA Paper 2001-2277, 7th AIAA/CEAS Aeroacoustics Conference, Maastricht, The Netherlands, 28-30 May, 2001.

8. Pritchard, Jocelyn, Pappa, Richard, Buehrle, Ralph and Grosveld, Ferdinand, "Comparison of Modal Analysis Methods Applied to a Vibro-Acoustic Test Article," Proceedings of the International Modal Analysis Conference, Los Angeles, CA, February 4-7, 2002.

Tables

Table 1: Aluminum Testbed Cylinder configurations

Configuration	I	II	III	IV	V	VI
Stringers	●	●	●	●	●	●
Frames	●	●	●	●	●	●
End Rings	●	●	●	●	●	●
End Plates		●		●	●	●
Skin			●	●	●	●
Domes					●	●
Internal Pressure						●

Table 2: Longitudinal stringer modal frequencies for a plate model and a refined plate model (twice the plate elements)

Stringer Mode shape	Measured Frequency	Predicted Frequency Plate Model	Error	Predicted Frequency Refined	Error
	(Hz)	(Hz)	%	(Hz)	%
x-z plane; j=1	8.8	9.2	3.9	9.1	2.8
y-z plane; j=1	9.4	9.7	3.4	9.8	3.7
x-z plane; j=2	24.5	25.2	2.9	24.9	1.8
y-z plane; j=2	26	25.9	-0.4	26.0	0.0
x-z plane; j=3	47.6	49.4	3.7	48.9	2.6
y-z plane; j=3	48.3	48.6	0.7	48.8	1.0
x-z plane; j=4	78.5	81.6	3.9	80.7	2.8
y-z plane; j=4	76.2	76.0	-0.3	76.3	0.1
x-z plane; j=5	117.2	121.8	3.9	120.4	2.7
y-z plane; j=5	109	106.6	-2.2	107.2	-1.6
x-z plane; j=6	163	170.0	4.3	167.9	3.0
y-z plane; j=6	145	139.8	-3.6	141.0	-2.7

Table 3: Ring frame modal frequencies for an updated hybrid model and a refined hybrid model (twice the plate elements)

Ring Frame Mode Shape	Measured Frequency	Predicted Frequency Updated Hybrid Model	Error	Predicted Frequency Refined Hybrid Model	Error
	[Hz]	[Hz]	[%]		[%]
Out-of-Plane	9.84	10.5	6.7	9.8	-0.5
n=2	9.84	10.5	6.7	9.8	-0.5
Out-of-Plane	31.47	33.2	5.6	31.2	-0.7
n=3	31.47	33.2	5.6	31.2	-0.7
Out-of-Plane	63.49	66.4	4.7	62.8	-1.1
n=4	63.49	66.4	4.7	62.8	-1.1
Out-of-Plane	104.81	108.4	3.5	102.8	-1.9
n=5	104.81	108.4	3.5	102.8	-1.9
Out-of-Plane	153.73	157.5	2.4	149.7	-2.6
n=6	153.73	157.5	2.4	149.7	-2.6
In-Plane	34.3	35.6	3.9	33.8	-1.4
i=2	34.3	35.6	3.9	33.8	-1.4
In-Plane	97.95	101.4	3.6	96.3	-1.7
i=3	97.95	101.4	3.6	96.3	-1.7
In-Plane	186.29	192.1	3.1	182.7	-2.0
i=4	186.29	192.1	3.1	182.7	-2.0

Table 4: S-fiberglass, epoxy matrix and lamina composite mechanical properties

Property	Units	S-fiberglass	Epoxy matrix	Lamina composite
Elasticity modulus	[psi]	E_f = 12,398,000	E_m = 500,000	E_{11} = 6,449,000
Elasticity modulus	[psi]			E_{22} = 1,698,000
Shear modulus	[psi]	G_f = 7,947,000	G_m = 357,100	G_{12} = 683,600
Poisson's ratio	[-]	v_f = 0.22	v_m = 0.30	v_{12} = 0.276
Volume percentage	[-]	V_f = 0.5	V_m = 0.5	V_c = 1.0
Specific weight	[pci]	$g\rho_f$ = 0.090	$g\rho_m$ = 0.045	$g\rho_c$ = 0.067

Table 5: Dome fiberglass laminate stacking sequence

Sequence	Material	Thickness	Orientation
[-]		[in]	[deg]
1	Fiberglass	0.004	0
2	Fiberglass	0.004	45
3	Fiberglass	0.026	0
4	Fiberglass	0.026	45
5	Fiberglass	0.026	0
6	Fiberglass	0.026	45
7	Fiberglass	0.026	0
8	Fiberglass	0.026	45
9	Fiberglass	0.026	0
10	Fiberglass	0.026	45
11	Fiberglass	0.026	0

Table 6: Measured modal frequencies of the ATC dome compared with predictions

Dome Mode Shape	Measured Frequency	Predicted Frequency	Error
	[Hz]	[Hz]	[%]
i=2 circumferential mode	21.6	21.3	-1.2
i=2 circumferential mode	21.6	21.3	-0.9
i=3 circumferential mode	68.7	64.8	-5.6
i=3 circumferential mode	68.7	64.8	-5.6
i=4 circumferential mode	135.5	129.3	-4.6
i=4 circumferential mode	135.5	129.4	-4.5
i=5 circumferential mode	224.0	213.5	-4.7
i=5 circumferential mode	224.0	213.5	-4.7
i=6 circumferential mode	321.6	316.0	-1.8
i=6 circumferential mode	321.6	316.0	-1.7

Table 7: Measured and predicted modal frequencies of the ATC Configuration I for unrefined and refined (twice the plate elements) models and for different number of nodes at the junctions of the longitudinal stringers and ring frames

Configuration I Mode Shape	Measured Frequency	Unrefined Predicted Frequency (12-node)	Unrefined Error (12-node)	Refined Predicted Frequency (30-node)	Refined Error (30-node)	Refined Predicted Frequency (6-nodes)	Refined Error (6-nodes)
	[Hz]	[Hz]	[%]	[Hz]	[%]	[Hz]	[%]
First torsion mode	9.9	11.0	11.1	7.6	-23.9	10.1	2.0
First x bending mode	16.3	18.7	14.9	14.1	-13.2	17.5	7.5
First y bending mode	16.8	18.7	11.8	14.1	-15.6	17.5	4.5
First x shearing mode	22.0	25.3	15.2	17.5	-20.3	23.4	6.8
First y shearing mode	22.6	25.3	12.2	17.5	-22.4	23.4	3.9
Second torsion mode	22.8	25.6	12.2	18.6	-18.3	23.7	4.1
i=2, j=1 circumferential-axial mode	29.4	29.7	1.1	26.7	-9.2	28.2	-4.0
i=2, j=1 circumferential-axial mode	29.4	29.7	1.0	26.7	-9.4	28.2	-4.2
Second x bending mode	31.5	36.2	14.8	29.4	-6.8	34.1	7.4
Second y bending mode	31.8	36.2	13.9	29.4	-7.5	34.1	6.5
i=2, j=2 circumferential-axial mode	34.2	35.6	4.0	31.5	-7.8	33.8	-1.1
i=2, j=2 circumferential-axial mode	34.4	35.6	3.3	31.5	-8.4	33.8	-1.8
Third torsion mode	38.5	44.4	15.1	34.3	-11.1	41.4	7.5
i=2, j=3 circumferential-axial mode	42.7	46.2	8.2	42.3	-0.9	44.1	3.4
i=2, j=3 circumferential-axial mode	43.0	46.2	7.4	42.3	-1.6	44.1	2.6
i=2, j=4 circumferential-axial mode	48.4	53.3	10.0	49.9	3.0	51.1	5.5
i=2, j=4 circumferential-axial mode	49.7	53.3	7.2	49.9	0.4	51.1	2.8

Table 8: Measured and predicted modal frequencies of ATC Configuration I with double the number of plate elements and a 12-noded junction at the location of the rivets

Configuration I Mode Shape	Measured Frequency	Predicted Frequency	Error
	[Hz]	[Hz]	[%]
First torsion mode	9.9	9.7	-2.6
First x bending mode	16.3	16.9	3.5
First y bending mode	16.8	16.9	0.7
First x shearing mode	22.0	22.3	1.7
First y shearing mode	22.6	22.3	-1.0
Second torsion mode	22.8	22.7	-0.3
i=2, j=1 circumferential-axial	29.4	28.0	-4.6
i=2, j=1 circumferential-axial	29.4	28.0	-4.8
Second x bending mode	31.5	33.1	5.1
Second y bending mode	31.8	33.1	4.3
i=2, j=2 circumferential-axial	34.2	33.5	-2.1
i=2, j=2 circumferential-axial	34.4	33.5	-2.7
Third torsion mode	38.5	40.0	3.7
i=2, j=3 circumferential-axial	42.7	43.3	2.7
i=2, j=3 circumferential-axial	43.0	43.8	2.0
i=2, j=4 circumferential-axial	48.4	50.9	5.1
i=2, j=4 circumferential-axial	49.7	50.9	2.5

Table 9: Measured and predicted modal frequencies of ATC Configuration II

Configuration II Mode Shape	Measured Frequency	Predicted Frequency	Error
	[Hz]	[Hz]	[%]
First bending	13.5	14.0	3.6
First bending	13.8	14.0	2.0
First torsion	19.6	19.8	1.2
Second bending	28.0	29.6	5.6
Second bending	28.1	29.6	5.1
i=2, j=1 circumferential-axial	29.5	28.1	-4.8
i=2, j=1 circumferential-axial	29.5	28.1	-5.0
i=2, j=2 circumferential-axial	34.8	34.3	-1.4
i=2, j=2 circumferential-axial	35.0	34.3	-2.1
Second torsion	36.2	37.5	3.7
i=2, j=3 circumferential-axial	46.3	47.6	2.9
i=2, j=3 circumferential-axial	46.4	47.6	2.7
Third bending		47.9	
Third bending		47.9	
Third torsion	57.1	59.24	3.6
i=2, j=4 circumferential-axial	62.3	66.63	6.5
i=2, j=4 circumferential-axial	62.9	66.63	5.5

Table 10: Measured and predicted modal frequencies of ATC Configuration III

Configuration III Mode Shape	Measured Frequency	Predicted Frequency	Error
	[Hz]	[Hz]	[%]
i=2, j=0 Rayleigh mode	50.8	52.4	3.2
i=2, j=0 Rayleigh mode	51.2	52.4	2.4
i=2, j=0 Love mode	53.5	56.3	5.2
i=2, j=0 Love mode	54.29	56.3	3.6
i=2, j=1 circumferential-axial	100.2	108.1	7.9
i=2, j=1 circumferential-axial	102.1	108.1	5.8
i=3, j=1 circumferential-axial	141.4	141.8	0.3
i=3, j=1 circumferential-axial	142.4	141.8	-0.4
i=3, j=2 circumferential-axial	152.4	157.2	3.1
i=3, j=2 circumferential-axial	152.4	157.2	3.1
i=3, j=3 circumferential-axial	160.1	169.0	5.6
i=3, j=3 circumferential-axial	161.8	169.0	4.4
i=3, j=4 circumferential-axial	183.6	192.9	5.1
i=3, j=4 circumferential-axial		192.9	
i=2, j=2 circumferential-axial	204.3	224.7	9.9
i=2, j=2 circumferential-axial	207.1	224.7	8.5
First x bending	224.6	228.7	1.9

Table 11: Measured and predicted modal frequencies of ATC Configuration IV

Configuration IV Mode Shape	Measured Frequency	Predicted Frequency	Error
	[Hz]	[Hz]	[%]
i=2, j=1 circumferential-axial	73.6	78.9	7.2
i=2, j=1 circumferential-axial	74.6	78.9	5.6
First axial mode	97.1	103.4	6.5
i=3, j=1 circumferential-axial	142.2	141.9	-0.2
i=3, j=1 circumferential-axial	143.3	141.9	-1.0
First x-bending mode	152.9	174.2	13.9
First y-bending mode		174.2	
i=3, j=2 circumferential-axial	167.9	173.6	3.4
i=3, j=2 circumferential-axial	169.9	173.6	2.2
First torsion		180.5	
i=2, j=2 circumferential-axial	174.8	192.9	10.4
i=2, j=2 circumferential-axial		192.9	
First xy-bending mode	195.7		
i=3, j=3 circumferential-axial	219.4	236.5	7.8
i=3, j=3 circumferential-axial	221.7	236.5	6.7
i=4, j=1 circumferential-axial	261.3	257.7	-1.4
i=4, j=1 circumferential-axial	264.1	257.7	-2.4

Table 12: Measured and predicted modal frequencies of ATC Configuration V

Configuration V Mode Shape	Measured Frequency	Predicted Frequency	Error
	[Hz]	[Hz]	[%]
i=2, j=1 circumferential-axial	79.1	86.42	9.2
i=2, j=1 circumferential-axial	79.9	86.85	8.7
First x bending mode	123.2	146.78	19.2
First y bending mode	124.2	147.62	18.9
First torsion mode	141.6	150.92	6.6
i=3, j=1 circumferential-axial	143.9	144.18	0.2
i=3, j=1 circumferential-axial	145.1	144.22	-0.6
i=2, j=2 circumferential-axial	166.3	199.20	19.8
i=2, j=2 circumferential-axial		199.42	
i=3, j=2 circumferential-axial	170.5	177.46	4.1
i=3, j=2 circumferential-axial	171.9	177.56	3.3
i=3, j=3 circumferential-axial	220.3	240.45	9.1
i=3, j=3 circumferential-axial	221.4	240.52	8.7
i=2, j=3 circumferential-axial	259.3	324.98	25.3
i=2, j=3 circumferential-axial		325.08	
i=4, j=1 circumferential-axial	261.5	258.87	-1.0
i=4, j=1 circumferential-axial	264.1	258.89	-2.0

Table 14. Predicted and measured modal frequencies of the ATC interior acoustic space.

Mode Number			Predicted Frequency	Measured Frequency
Axial	Circumferential	Radial		
[-]	[-]	[-]	[Hz]	[Hz]
1	0	0	47.6	51
2	0	0	95.4	97
3	0	0	143.6	143
0	1	0	165.2	
0	1	0	165.2	
1	1	0	171.9	
1	1	0	171.9	
2	1	0	190.8	
2	1	0	190.8	
4	0	0	192.4	190
3	1	0	218.9	
3	1	0	218.9	
5	0	0	242.0	238
4	1	0	253.6	
4	1	0	253.6	
0	2	0	274.4	
0	2	0	274.6	

Table 13: Measured and predicted modal frequencies of ATC Configuration VI for 0 and 6 psi pressurization.

Configuration VI Mode Shape	Measured Frequency 0 psi	Measured Frequency 6 psi	Measured Difference	Predicted Difference	Predicted Frequency 0 psi	Predicted Frequency 6 psi
	[Hz]	[Hz]	[%]	[%]	[Hz]	[Hz]
i=2, j=1 circumferential-axial mode	79.1	82.3	3.9	4.7	86.4	90.5
i=2, j=1 circumferential-axial mode	79.9	82.9	3.8	4.7	86.9	90.9
First x bending	123.2	121.5	-1.4	0.1	146.8	147.0
First y bending	124.2	123.0	-1.0	0.1	147.6	147.8
First torsion	141.6	141.1	-0.3	-0.2	150.9	150.6
i=3, j=1 circumferential-axial mode	143.9	150.6	4.7	4.9	144.2	151.2
i=3, j=1 circumferential-axial mode	145.1	151.9	4.7	4.9	144.2	151.3
i=2, j=2 circumferential-axial mode	166.3	169.5	1.9	1.4	199.2	202.0
i=2, j=2 circumferential-axial mode				1.4	199.4	202.3
i=3, j=2 circumferential-axial mode	170.5	176.1	3.3	3.6	177.5	183.8
i=3, j=2 circumferential-axial mode	171.9	177.4	3.2	3.6	177.6	183.9
i=3, j=3 circumferential-axial mode	220.3	225.7	2.4	2.6	240.5	246.7
i=3, j=3 circumferential-axial mode	221.4	226.4	2.3	2.6	240.5	246.7
i=2, j=3 circumferential-axial mode	259.3	261.6	1.0	2.2	325.0	332.2
i=2, j=3 circumferential-axial mode				2.2	325.1	332.2
i=4, j=1 circumferential-axial mode	261.5	268.8	2.8	2.9	258.9	266.5
i=4, j=1 circumferential-axial mode	264.1	272.1	3.0	2.9	258.9	266.5

Figures

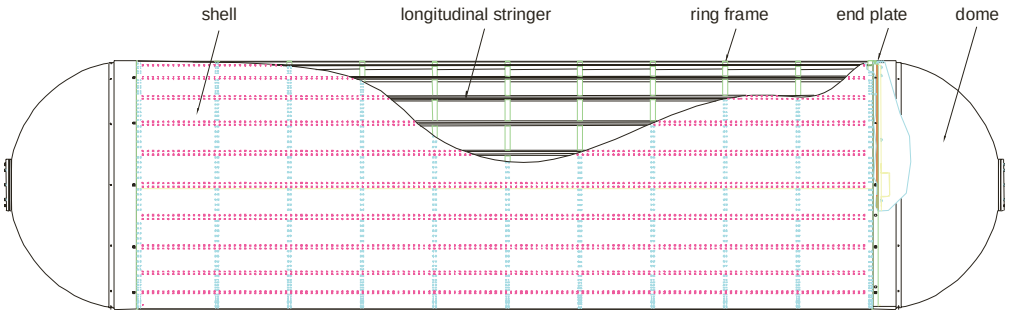

Figure 1. Aluminum Testbed Cylinder (ATC) showing the stringers, frames, end plates, shell and domes

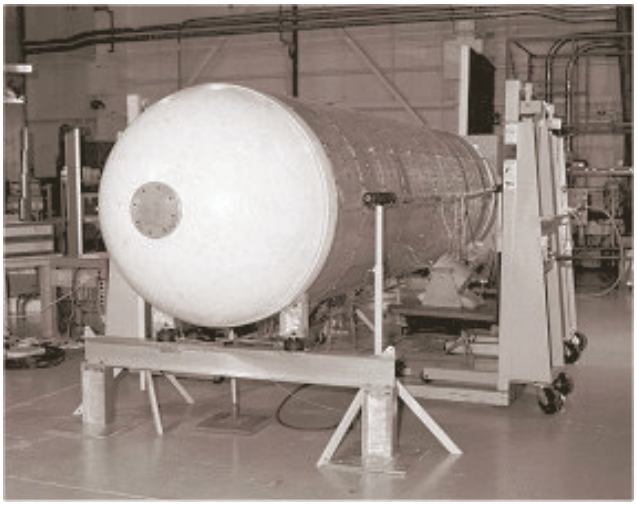

Figure 2. Test setup of ATC Configuration V

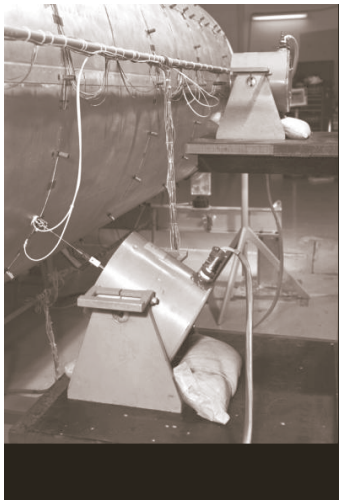

Figure 3. Shaker used for modal testing

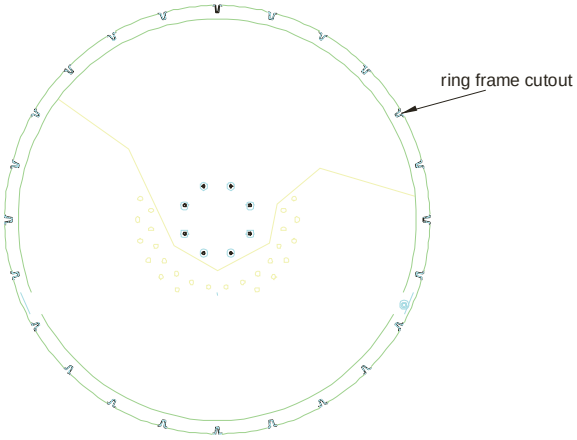

Figure 4. ATC ring frame showing the twenty-four cutouts to accommodate the longitudinal stringers

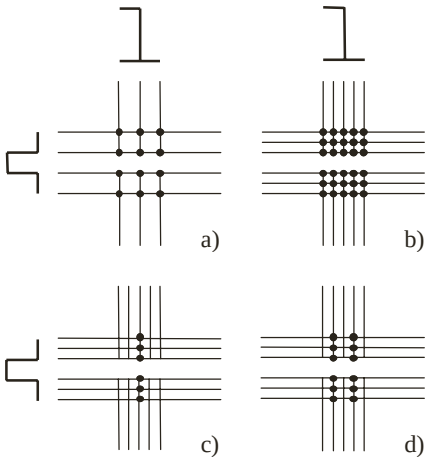

Figure 5. Schematic top view of the hat-section stringer and the J-section ring frame connections showing mutual nodes.